21 Jan 2021

Fully-Kinetic Particle-In-Cell Simulations of Photoelectron Sheath on Uneven Lunar Surface

Jianxun Zhao

Xinpeng Wei

Xiaoming He
Missouri University of Science and Technology, hex@mst.edu

Daoru Frank Han
Missouri University of Science and Technology, handao@mst.edu

et. al. For a complete list of authors, see https://scholarsmine.mst.edu/math_stat_facwork/1018

Recommended Citation

J. Zhao et al., "Fully-Kinetic Particle-In-Cell Simulations of Photoelectron Sheath on Uneven Lunar Surface," *Proceedings of the AIAA Scitech 2021 Forum*, pp. 1-14, American Institute of Aeronautics and Astronautics (AIAA), Jan 2021.
The definitive version is available at https://doi.org/10.2514/6.2021-1433

AIAA SciTech Forum
11–15 & 19–21 January 2021, VIRTUAL EVENT
AIAA Scitech 2021 Forum

10.2514/6.2021-1433

Fully-Kinetic Particle-in-Cell Simulations of Photoelectron Sheath on Uneven Lunar Surface

Jianxun Zhao*, Xinpeng Wei†, Xiaoming He‡, and Daoru Han§
Missouri University of Science and Technology, Rolla, Missouri 65409

Xiaoping Du¶
Indiana University - Purdue University Indianapolis, Indianapolis, Indiana 46202

This paper presents a modeling and simulation study of the photoelectron sheath near uneven lunar surface. A fully kinetic 3-D finite-difference (FD) particle-in-cell (PIC) code is utilized to simulate the plasma interaction with local uneven surface terrain on the lunar surface in 2-D photoelectron sheaths. The code is first validated using a 1-D plasma charging and sheath problem by comparing with a semi-analytic solution. Good agreement is obtained. The 2-D FD-PIC simulations present the distributions of electric potential and charged species densities near the uneven lunar surface. It shows that the surface potential is highly influenced by the exposure to sunlight and local Sun elevation angle. Under average solar wind conditions, exposure to sunlight could lead to a positive surface potential with a magnitude of tens of volts, whereas the lack of sunlight results in a negative surface potential of several volts.

I. Nomenclature

e = elementary charge
m = mass
n = density
k = Boltzmann constant
T = temperature
v = velocity

Greek letters
ϕ = electric potential
ε = relative permittivity

Subscript
phe = photoelectron
ref = reference

II. Introduction

The lunar surface is directly exposed to the solar radiation and solar wind plasma due to the lack of protection of the global atmosphere and magnetic field. The interaction between the lunar surface and the charged particles leads to a charging process on the lunar surface, causing a negative or positive surface electric potential with respect to the ambient environment. The charging process on the lunar surface has been studied extensively [1–15]. In this paper, we focus on the 2-D structure of the photoelectron sheath and its effects on local uneven surface terrain. A fully kinetic

*Graduate Research Assistant, Department of Mechanical and Aerospace Engineering, 400 W. 13th St., Rolla, MO 65409, AIAA Student Member.
†Graduate Research Assistant, Department of Mechanical and Aerospace Engineering. 400 W. 13th St., Rolla, MO 65409.
‡Associate Professor, Department of Mathematics and Statistics. 400 W. 12th St., Rolla, MO 65409.
§Assistant Professor, Department of Mechanical and Aerospace Engineering, 400 W. 13th St., Rolla, MO 65409, AIAA Member. handao@mst.edu
¶Professor, Purdue School of Engineering and Technology, 799 W. Michigan St., Indianapolis, IN 46202.

3-D finite-difference (FD) particle-in-cell (PIC) code [7, 16] is utilized to simulate the plasma interaction near the lunar surface. The FD-PIC code is first validated by comparing the numerical results with semi-analytic solutions for a 1-D charging and sheath problem. Then we consider the 2-D surface terrain in two cases. The first case includes a rectangular building and the second case represents a rectangular pit. Both cases represent possible landscapes of lunar surface infrastructure for a future lunar base or colony. The objective of this study is to provide insight of potential hazard caused by electric discharge due to large differential charging near these surface infrastructures. The rest of this paper is organized as follows. Section III introduces the photoelectron sheath model and the validation of the FD-PIC code. Section IV presents the results of numerical simulation of the 2-D photoelectron sheath structure. Conclusions are given in Section V.

III. Sheath Model and Code Validation

A. Sheath Model

The essential part of the semi-analytic solution of 1-D photoelectron sheath in this study follows [1] and [4]. According to [1] and [4], there are 3 possible types of potential profiles in the photoelectron sheath: Type A, Type B, and Type C, as shown in Fig. 1. For each sheath type, the populations of electrons are different. The solar wind electron population contains "free solar wind electrons", representing electrons which are able to reach the lunar surface, and "reflected solar wind electrons", representing electrons that are reflected by the potential barrier. The photoelectron population contains "free photoelectrons", representing those able to reach the infinity, and "captured photoelectrons", representing those attracted back to the lunar surface, due to the positive surface potential.

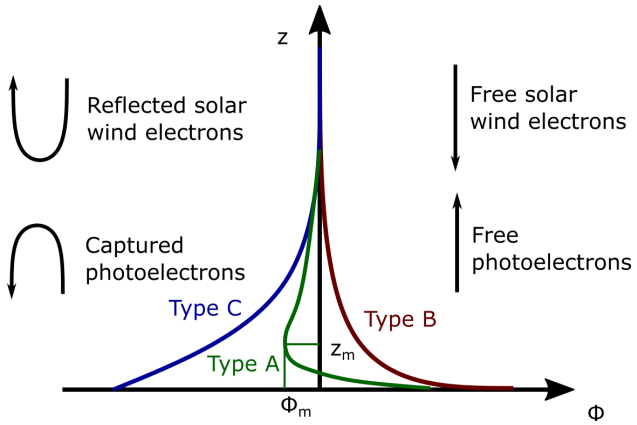

Fig. 1 Different populations of electrons as described in [4]

Among these three types of profile, Type A is a non-monotonic potential profile, the curve of Type A first decreases from the surface to the minimum potential, then it increases to the potential at infinity, which is assumed to be zero. It is believed that non-monotonic potential profiles have lower electrostatic energy than their monotonic counterparts, therefore representing the more stable states [4, 10]. This hypothesis is then evidenced by measurements from the Lunar Prospector [9] and the ARTEMIS missions [11]. Both Type B and Type C are monotonic. The curve of Type B decreases from the surface potential to zero. Whereas the curve of Type C increases from the surface potential to zero.

The type of the photoelectron sheath largely depends on the Sun elevation angle. In this study, we focus on the sheath structure at lunar terminator regions where Sun elevation angles are low. Thus, it is believed that the Type C photoelectron sheath will occur on the flat surfaces. However, it is noted here that the Sun elevation angle may be greater at local uneven places such as vertical surfaces, which can result in a more complex potential profile near these surfaces.

B. Validation of the FD-PIC Code

In this section we validate the FD-PIC code by comparing the numerical results with semi-analytic solutions introduced in [17, 18] before conducting the 2-D numerical simulations. We consider a 1-D planar charging and sheath problem with cold drifting ions and thermal electrons in this validation case, and compare the 1-D potential profile with the semi-analytic solution.

1. Plasma Conditions

The plasma species in the validation case include cold drifting ions and thermal electrons for the average solar wind condition as considered in our previous studies [7, 16, 19] and used in Section IV. The cold drifting ions travel perpendicular to the surface with a drifting velocity of 468 km/s. The electrons are considered as thermal with a temperature of 12 eV. The density of both electrons and ions are 8.7 cm^{-3}. The parameters of solar wind species are listed in Table 1. It is noted here that for the validation case, we used parameters of solar wind electrons as the normalization reference.

Table 1 Solar wind parameters

	Solar wind electrons	Solar wind ions
Drifting Velocity, km/s	468	468
Density, cm^{-3}	8.7	8.7
Temperature, eV	12	0

2. Computation Domain and Boundary Conditions

In this validation case, the computation domain has 2×2×20 PIC cells, with an object with height of 2 PIC cells located on the surface, as shown in Fig. 2(a). The vacuum relative permittivity is set as 1.0 (normalized by the vacuum permittivity ε_0), whereas the object and ground relative permittivity are both set as 4.0, as shown in Fig. 2(b).

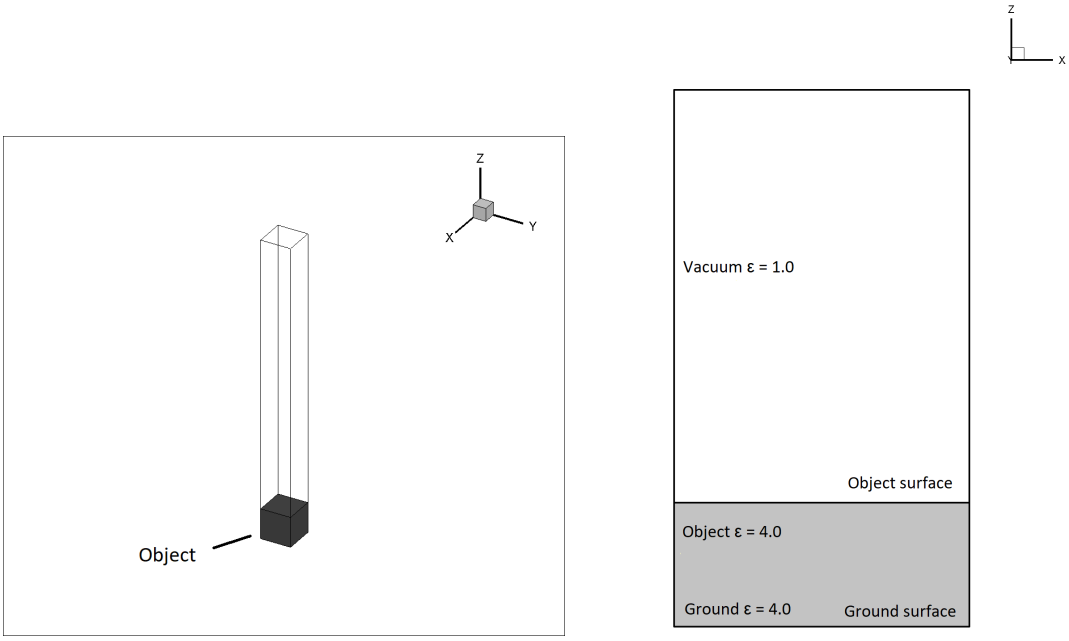

(a) Overall computation domain (b) Permittivities in computation domain

Fig. 2 Computation domain of the validation case

Both the ground surface and the object surface are set as “absorb”, which means once the electrons or ions hit these surfaces, the particle will deposit and the charge will be accumulated on the surface. The surrounding boundaries are set as “reflective”, thus once the particle travels across the boundary, it will be reflected back with an opposite direction of the velocity component which is perpendicular to the boundary. The top surface of the computation domain, where is considered as infinity with a zero electric potential, is set as “inject”, from where the solar wind ions and electrons enter the computation domain. The parameters utilized in validation case are listed in Table 2.

Table 2 Computation domain parameters (BC means boundary condition)

Vacuum ε	Building ε	Ground ε	Surrounding BC	Bottom BC	Top BC
1.0	4.0	4.0	reflective	absorb	inject

3. Results and Comparisons

The comparison of the numerical result and the semi-analytic solution of the validation case is shown in Fig. 3. As it can be seen, good agreement is obtained. According to the comparison, the potential in most areas above the surface in the computation domain is nearly zero, due to the neutrality of the solar wind density (solar wind electrons together with solar wind ions). The negative potential above the surface is caused by the larger amount of solar wind electrons accumulated on the surface compared with solar wind ions, due to the higher thermal velocity of the solar wind electrons. The good agreement of the numerical result and the semi-analytic solution validated the accuracy of the FD-PIC code.

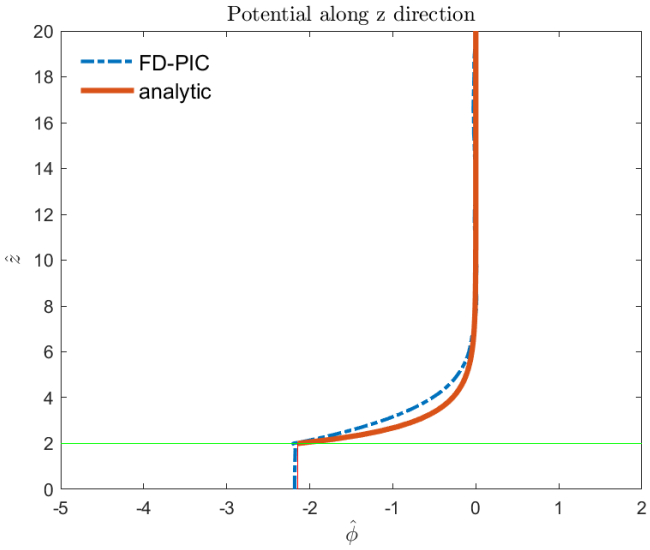

Fig. 3 Comparison of numerical result and semi-analytic solution, the green line represents the surface

IV. 2-D Structures of Photoelectron Sheath

A. Setup of Numerical Simulation

In this section we will study the 2-D structures of photoelectron sheath above the lunar surface. Two types of structures were simulated: one with a rectangular building located on the lunar surface as shown in Fig. 4 (Case 1); the other with a rectangular pit on the lunar ground as shown in Fig. 5 (Case 2).

1. Solar Wind Conditions

The solar wind conditions are set to be the same as in Section III.B.1, except including a horizontal component of solar wind velocity at an angle of 10° towards the lunar surface for the polar region. The photoelectron is also considered in this case with a temperature of 2.2 eV. The parameters of the solar wind and photoelectrons are listed in Table 3.

2. Normalization

For the 2-D simulations, parameters of photoelectron are used as normalization reference as listed in Table 4, where λ_d is the Debye length of photoelectron at 90° Sun elevation angle; T_{phe} is the temperature of the photoelectron; m_{phe}

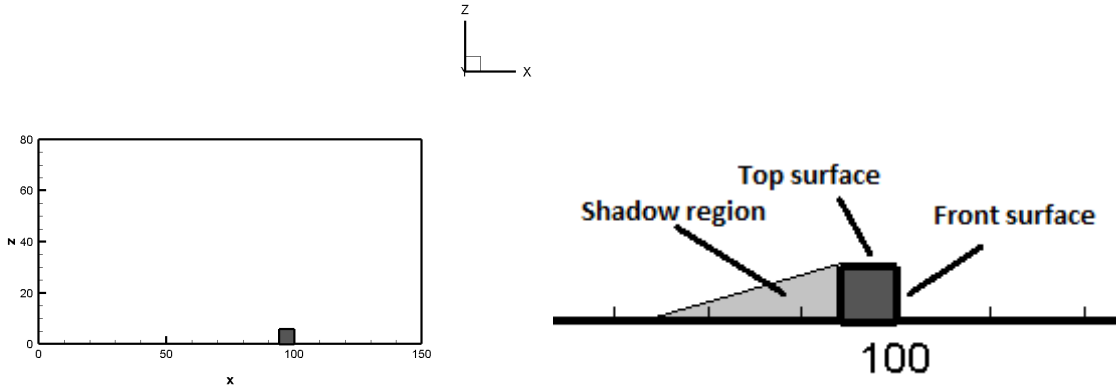

(a) Computation domain (b) Details of Case 1

Fig. 4 Case 1: A rectangular building

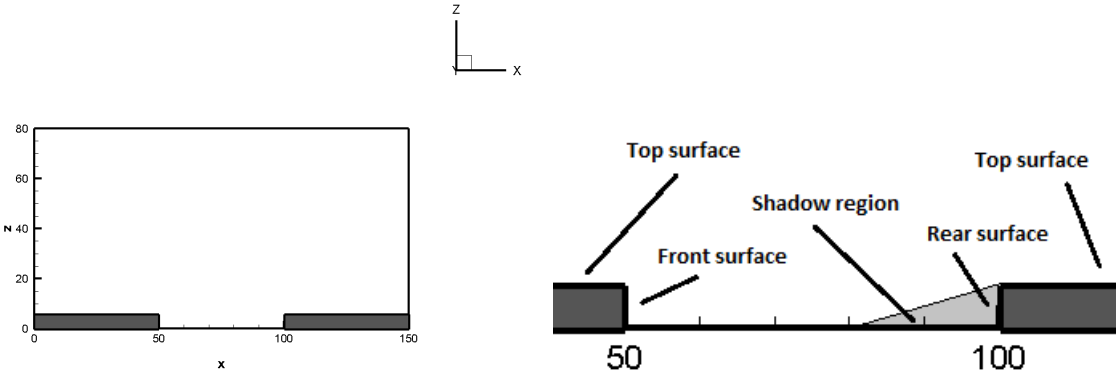

(a) Computation domain (b) Details of Case 2

Fig. 5 Case 2: A rectangular pit

Table 3 Solar wind parameters of Cases 1 and 2 (where α is the Sun elevation angle)

	Solar wind electrons	Solar wind ions	Photoelectrons
Drifting Velocity, km/s	468	468	-
Density, cm^{-3}	8.7	8.7	64 $\sin(\alpha)$
Temperature, eV	12	0	2.2

is the mass of the photoelectron; k is the Boltzmann constant; e is the electric charge; $v_{\mathrm{phe,t}} = \sqrt{kT_{\mathrm{phe}}/m_{\mathrm{phe}}}$ is the reference for velocity. and $n_{\mathrm{phe,ref}}$ is the photoelectron number density at 90° Sun elevation angle. The PIC time is normalized by $1/\omega_{\mathrm{phe}}$, where ω_{phe} is the plasma frequency of the photoelectron at normal incidence condition (90°).

3. Computation Domain and Boundary Conditions

In Case 1, the rectangular building with dimension of 6×2×6 PIC cells (physical dimension of 8.28×2.76×8.28 m) is located on a flat lunar surface with a shadow region behind, as shown in Fig. 4(b). Whereas in Case 2, the rectangular pit with dimension of 50×2×6 PIC cells (physical dimension of 69.0×2.76×8.28 m) is located in the center of the lunar

Table 4 Normalization references

L_{ref}	T_{ref}	m_{ref}	ϕ_{ref}	v_{ref}	n_{ref}	t_{ref}
λ_d	T_{phe}	m_{phe}	$\frac{kT_{\text{phe}}}{e}$	$v_{\text{phe,t}}$	$n_{\text{phe,ref}}$	$\frac{1}{\omega_{\text{phe}}}$

surface (with thickness of 8.22 m), and nearly half of the bottom surface inside the pit is covered by shadow, as shown in Fig. 5(b). The dimension of the computation domain for both two cases are set as 150×2×80 total PIC cells (physical dimension of 207.0×2.76×110.4 m).

The solar wind electrons and ions are traveling into the computation domain in the X-Y plane, along -z-direction. 1,800,000 macro particles representing each of solar wind electrons and ions are preloaded into the computation domain at the beginning of the simulation (total 3,600,000 macro particles), and another ~6,000 particles for each of solar wind electrons and ions, and ~7,500 particles for photoelectrons are injected into the computation domain in each time step. The simulations run 50,000 steps for each case, which is ~900 seconds in physical time. The wall clock time is ~6 hours for each run.

Zero-Dirichlet boundary condition where $\phi = 0$ is applied for the $Z_{\max}$ boundary, where is considered as infinity in the numerical simulation. The other boundaries are all applied with the zero-Neumann boundary condition where $\frac{\partial \phi}{\partial n} = 0$.

The particle boundary condition at $X_{\min}$ and $X_{\max}$ is set as "periodic", which means once the particle travels across the boundary, it will enter the computation domain from the opposite boundary with the same velocities, thus the whole domain is able to represent a relatively large area with low computation cost. The boundary condition at $Y_{\min}$ and $Y_{\max}$ is set as "reflective". The bottom surface (lunar surface and building surface) is set as "absorb", and the top surface of computation domain is set as "inject". The relative permittivity of the ground and the building is set to be the same as that in the validation case in Section III.B.2. The parameters of the computation domain are listed in Table 5.

Table 5 Computation domain parameters for 2-D structure

Vacuum ε	Building ε	Ground ε	BC along x	BC along y	Bottom BC	Top BC
1.0	4.0	4.0	reflective	periodic	absorb	inject

B. Simulation Results and Discussion

1. Case 1

The distribution of potential, densities, and E field for Case 1 are shown in Fig. 6 and 7. In Case 1, it can be seen that the potential is nearly zero in most areas above the surface, due to the charge neutrality in these areas (see Fig. 7(a)). The emission of photoelectrons from the building and ground surfaces, caused by the exposure to sunlight, leads to a positive potential on the front and top surface of the building and the ground surface outside the shadow region, whereas the lack of sunlight caused a negative potential on the dark side of the building and on the ground surface inside the shadow region. It is reasonable that the front surface of the building has a much higher potential, because of the larger photoelectron emission under greater local sunlight incidence angle. The numerical result shows that, the presence of sunlight can create a differential potential as large as tens of volts between the sunlit and shadow sides of a building located at lunar terminator regions with low Sun elevation angle.

Figure 7 shows densities of different species and E field in the computation domain for Case 1 (7(a): Total density; 7(b): Solar wind electron density; 7(c): Solar wind ion density; 7(d): Photoelectron density; and 7(e) and 7(f): E field in X-Z plane). It can be seen from Fig. 7(a) that the total density is nearly neutral in most areas above the bottom surface, which leads to a near-zero potential region in these areas (see Fig. 6).

The solar wind electron density is lower inside and above the shadow region (Fig. 7(b)), because the electrons within this region are easily hitting and depositing on the ground and building surfaces, leading to a negative surface potential. The negative surface potential then repels the nearby electrons, creating a region with lower electron density.

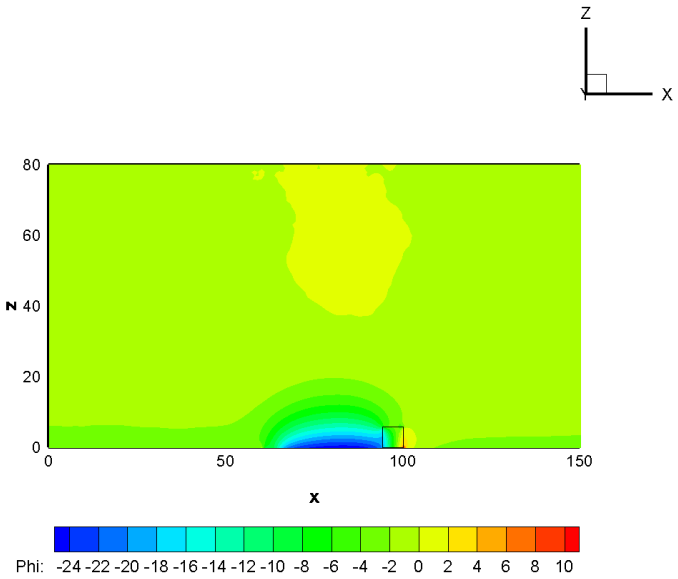

Fig. 6 Potential in Case 1 (normalized by 2.2 V)

On the other hand, the solar wind ions skip the shadow region behind the building and create a clear wake of ion void region (Fig. 7(c)), due to the "cold" temperature and larger mass of solar wind ions.

The photoelectrons are generated from the ground and building surfaces due to exposure to sunlight. The greater Sun elevation angle on the front surface results in a larger photoelectron emission, whereas in the shadow region behind the building, the photoelectron density is nearly zero (Fig. 7(d)).

The charge accumulation on the bottom surface leads to an electric field as shown in Fig. 7(e). The range of the electric field is from ~-5 V/m in the shadow region to ~10 V/m near the front surface of the building. It is believed that the electric field inside the building, as shown in Fig. 7(f), is controlled by both surface charge accumulation and the permittivity of the building material.

We also analyzed the potential profiles along z at different locations along x. Figure 8 shows the potential profiles at locations of $\hat{x}$ = 20, 50, 70, 96, 101, and 125. It can be seen that the potential profiles are similar at locations where are relatively far away from the building and the corresponding shadow region (see Fig. 8(a) and 8(f)). The potential gradient near the top surface is likely caused by the perturbation of the photoelectrons. The photoelectrons emitted from the exposed surfaces lead to a non-zero photoelectron density above these surfaces (as shown in Fig. 7(d)). The non-zero photoelectron density will then lead to a relatively negative potential. On the other hand, the potential is nearly zero in the region with no photoelectrons (the middle region in Fig. 7(d)), due to the charge neutrality (see Fig. 8(c)). The large density of photoelectron near the front surface of the building, together with the high thermal velocity, results in a highly "irregular" potential profile compared with that in other regions, as shown in Fig. 8(e).

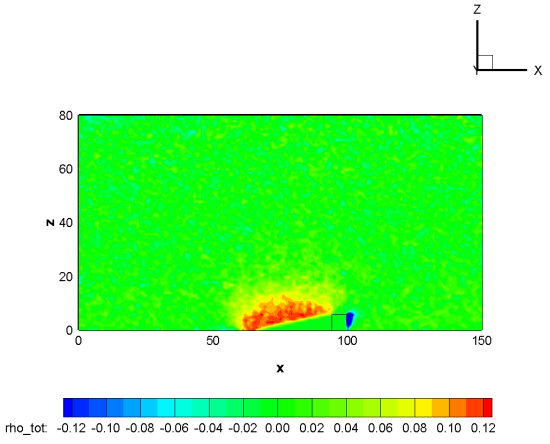

(a) Total density

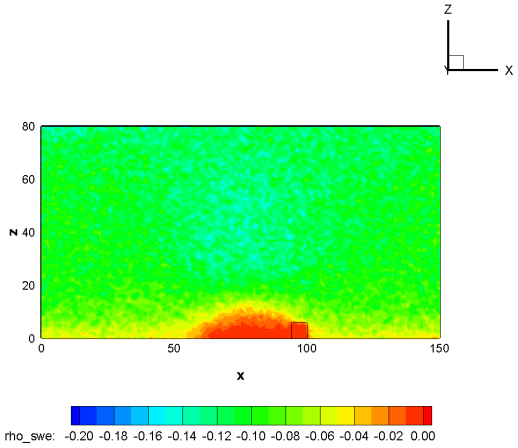

(b) Solar wind electron density

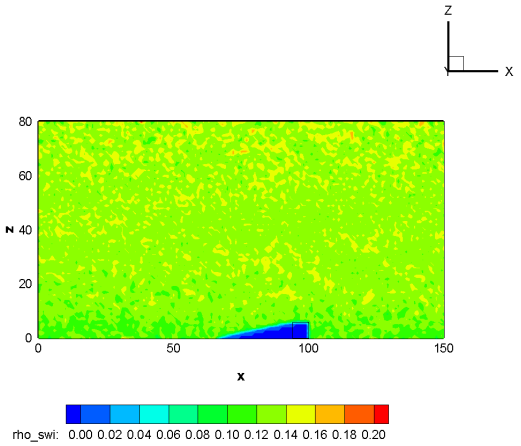

(c) Solar wind ion density

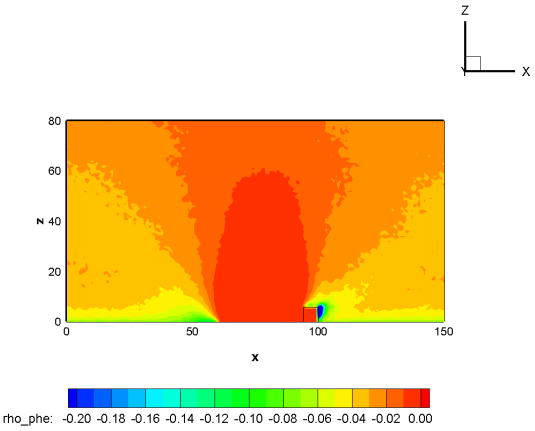

(d) Photoelectron density

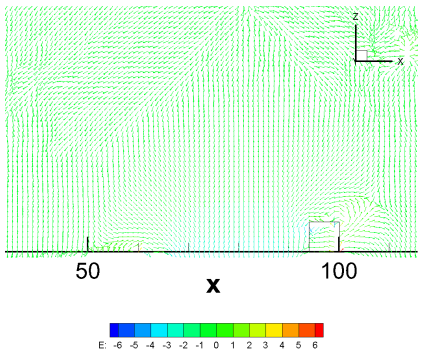

(e) E field vectors near building in X-Y plane

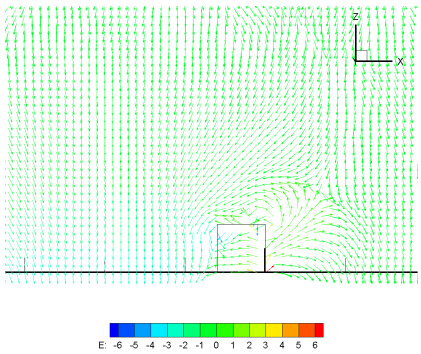

(f) E field vectors inside the shadow region and building

Fig. 7 Densities of solar wind and photoelectrons (normalized by 64 cm^{-3}) and E field (normalized by 1.59 V/m) in Case 1

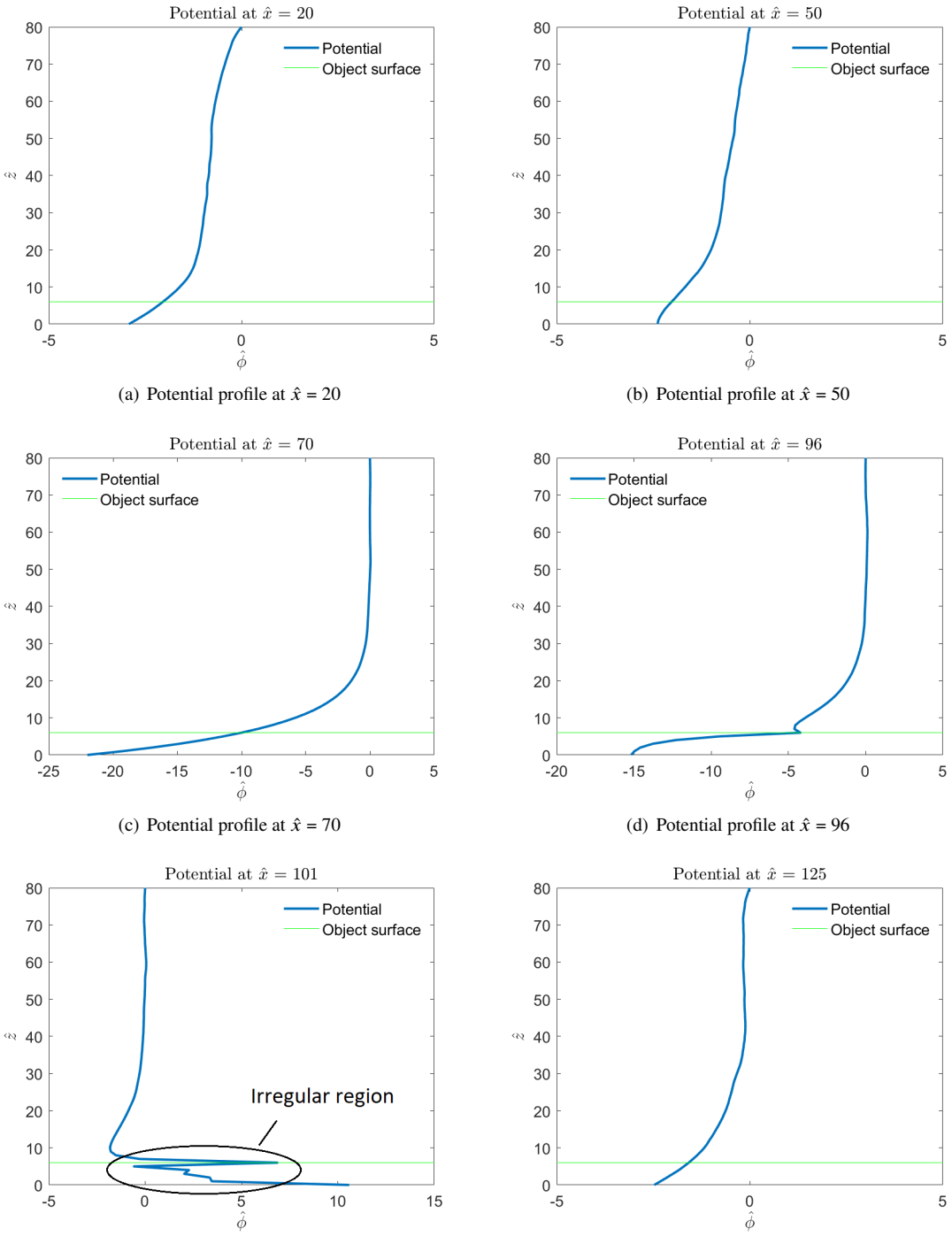

(a) Potential profile at $\hat{x}$ = 20

(b) Potential profile at $\hat{x}$ = 50

(c) Potential profile at $\hat{x}$ = 70

(d) Potential profile at $\hat{x}$ = 96

(e) Potential profile at $\hat{x}$ = 101

(f) Potential profile at $\hat{x}$ = 125

Fig. 8 Potential profile of Case 1 at different locations along x

2. Case 2

The simulation results of Case 2 representing the surface structure of a rectangular pit on the Moon, are in Fig. 9 to 11. Similarly, the potential is nearly zero above the surface in most areas, due to the charge neutrality of the total density. The surface potential outside the pit is negative of several volts (see Fig. 11(a), 11(b), 11(e) and 11(f)), due to the emission of photoelectrons. The magnitude of potential inside the rectangular pit depends on the size of the shadow region. In this specific case, the shadow region is not large enough to cover the entire bottom surface inside the pit, hence the bottom surface potential outside the shadow region is negative of several volts (see Fig. 7), whereas the bottom surface potential inside the shadow region is more negative with a magnitude of tens of volts (see Fig. 11(d)), caused by the deposition of solar wind electrons on this surface, which leads to a negative charge accumulation, and the lack of sunlight, which leads to the absence of photoemission in this region.

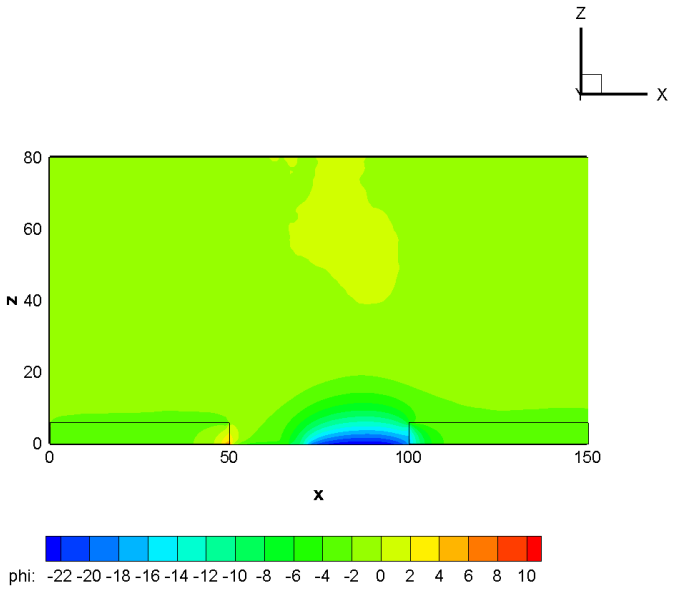

Fig. 9 Potential in Case 2 (normalized by 2.2 V)

The densities in Case 2 are also similar to those in Case 1. It can be seen in Fig. 10(a), the total charge density is nearly zero in most areas above the bottom surface, leading to near-zero potential region (see Fig. 9). The density is slightly positive above the shadow region inside the pit (see Fig. 10(a)), because the negatively charged bottom surface in the shadow region repels solar wind electrons nearby, creating a region with more ions. This is also demonstrated in solar wind electron density contour as shown in Fig. 10(b). The solar wind ions travel mostly in a straight line (as a cold beam), leading to a triangular region which is empty of ions in the shadow region inside the pit, as shown in Fig. 10(c). A "photoelectron void region" above the shadow region inside the pit is observed (see Fig. 10(d)), which is caused by the lack of sunlight on the bottom surface in the shadow region.

The range of the electric field is from ~-6 V/m in the shadow region inside the pit to ~10 V/m in front of the sunlit surface, as shown in Fig. 10(e) and 10(f).

The potential profiles along z at different locations, as shown in Fig. 11, present the potential structure of the photoelectron sheath in Case 2. Similar to Case 1, the potential profiles are quite similar in the areas where are relatively far away from the pit, due to the stable solar wind and photoelectron densities in these areas (see Fig. 11(a), 11(b), 11(e) and 11(f)). The potential gradient near the top of the computation domain is also caused by the photoelectrons originated from the exposed surfaces.

The potential near the front vertical surface (see Fig. 5) inside the pit shows a highly "irregular" potential profile (see Fig. 11(c)), due to the large amount of photoelectrons here. There are almost no photoelectrons above and inside the shadow region (see Fig. 10(d)), leading to a more "regular" potential profile as shown in Fig. 11(d).

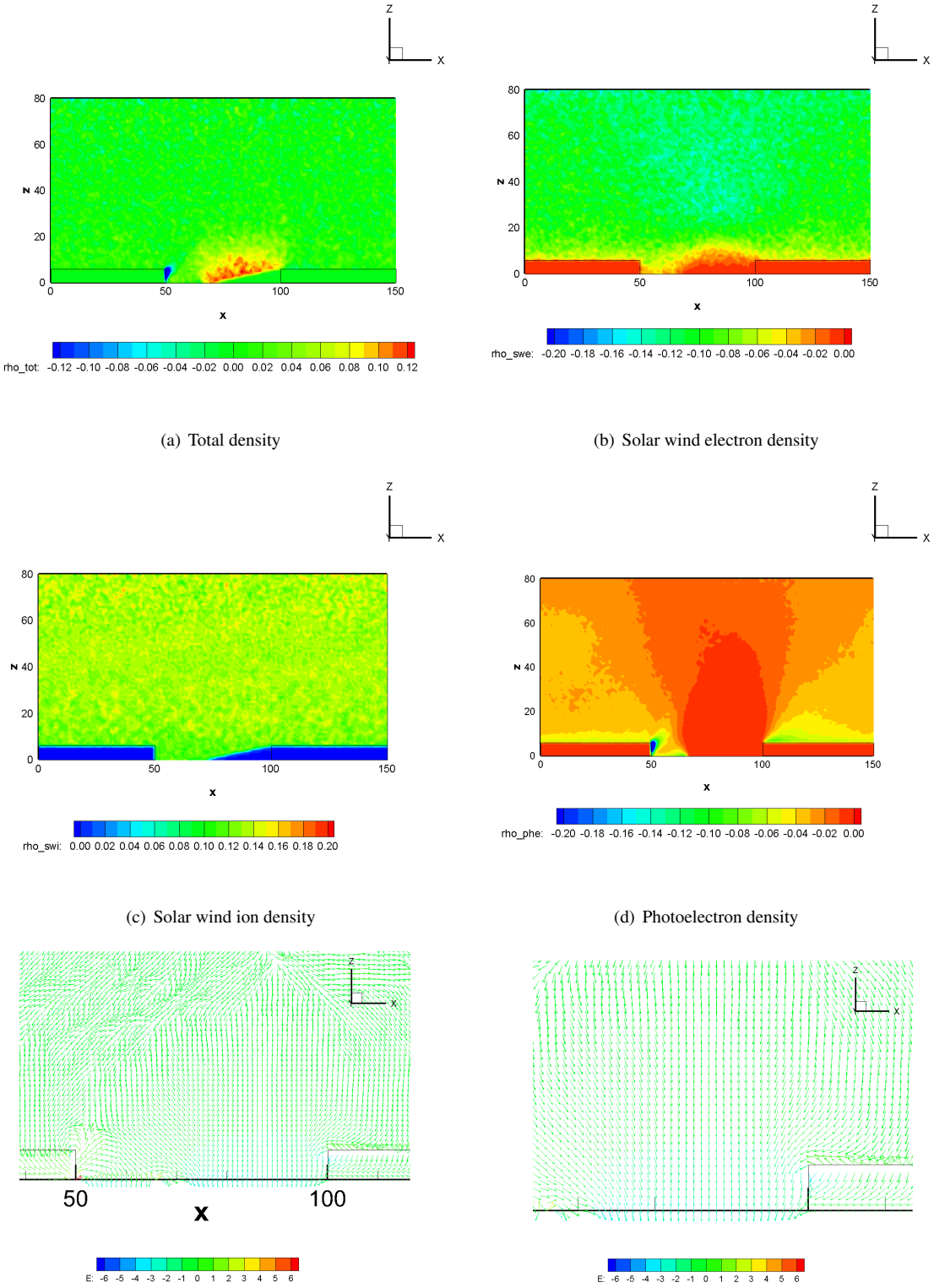

(a) Total density

(b) Solar wind electron density

(c) Solar wind ion density

(d) Photoelectron density

(e) E field vectors near pit in X-Y plane

(f) E field vectors inside shadow region

Fig. 10 Densities of solar wind and photoelectrons (normalized by 64 cm^{-3}) and E field (normalized by 1.59 V/m) in Case 2

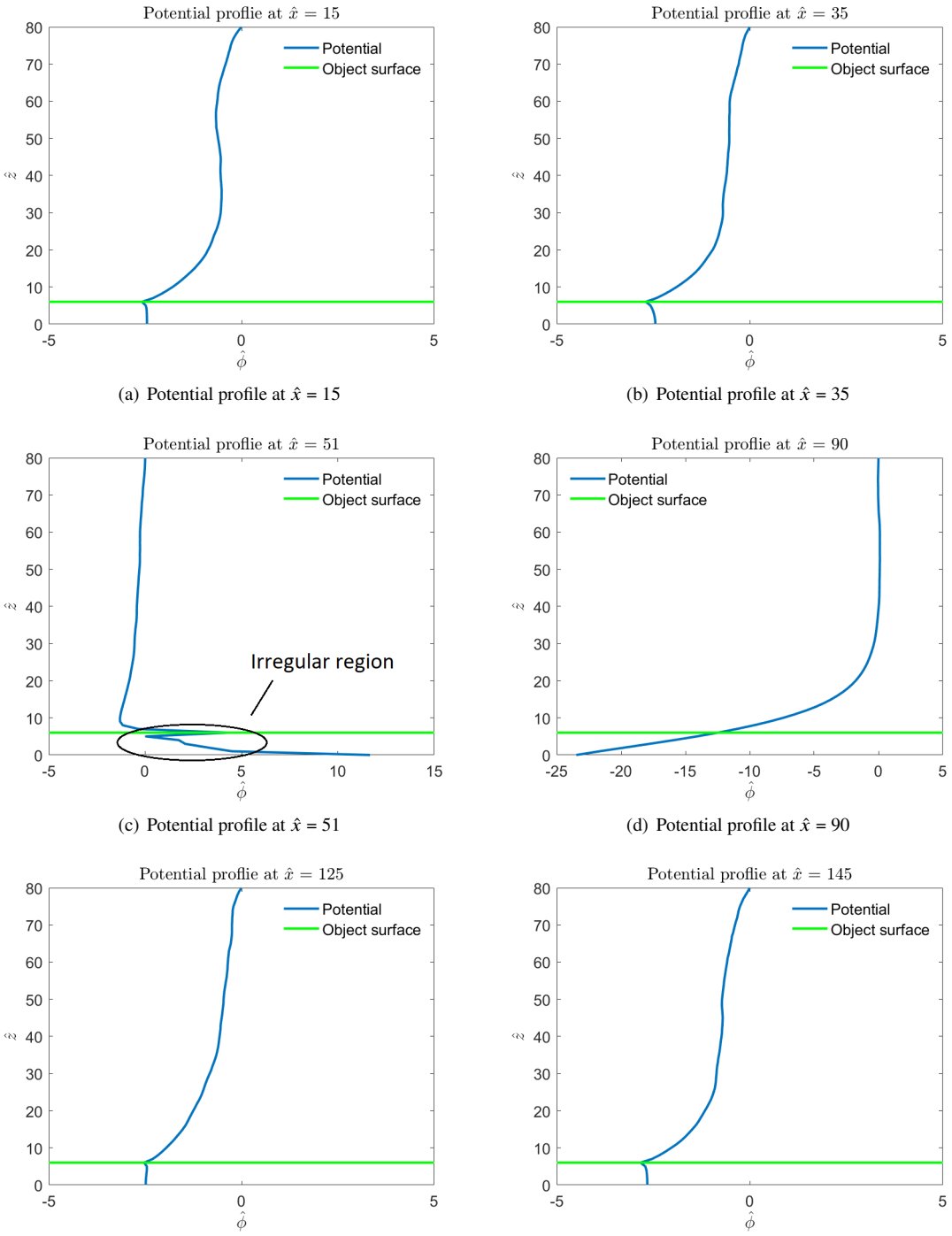

(a) Potential profile at $\hat{x}$ = 15

(b) Potential profile at $\hat{x}$ = 35

(c) Potential profile at $\hat{x}$ = 51

(d) Potential profile at $\hat{x}$ = 90

(e) Potential profile at $\hat{x}$ = 125

(f) Potential profile at $\hat{x}$ = 145

Fig. 11 Potential profile of Case 2 at different locations along x

V. Conclusion

We conducted a series of numerical simulations and presented the 2-D photoelectron sheaths at lunar terminator region (region with low Sun elevation angles) on the lunar surface for two surface terrains: One with a rectangular building located on a flat surface and the other with a rectangular pit on the lunar surface. The numerical results showed that the exposure to the sunlight and the Sun elevation angle play important roles on the surface potential and differential charging between the surface infrastructure and the ambient environment. The higher the local Sun incidence angle is, the larger the surface potential will be, due to the greater photoemission caused by sunlight. The vertical sunlit surfaces have more positive surface potentials compared with horizontal surfaces at terminator regions with low Sun elevation angle.

The density of solar wind and photoelectrons will affect the shape of potential profiles. The profile becomes more "irregular" in front of the sunlit vertical surface, due to the larger amount of photoelectrons. The charge accumulation on the building and ground surfaces will lead to a differential electric field with a range from several V/m negative in the shadow region to over 10 V/m on sunlit surfaces.

Ongoing work is to extend our investigation to include a larger range of Sun elevation angles in numerical simulations, and study the influence of the Sun elevation angle on the 2-D photoelectron sheath structures. We are also scaling up the FD-PIC code to simulate and study 3-D photoelectron sheath structures. Future work is planned to study the dust levitation/transport in these scenarios.

Acknowledgments

We would like to thank Prof. Joseph Wang of the University of Southern California for many helpful discussions. This work is financially supported in part by NASA-Missouri Space Grant Consortium through NASA-EPSCoR Missouri, and NSF-CMMI # 1923799.

References

[1] Fu, J. H. M., "Surface potential of a photoemitting plate," Journal of Geophysical Research (1896-1977), Vol. 76, No. 10, 1971, pp. 2506–2509. doi:10.1029/JA076i010p02506, URL https://agupubs.onlinelibrary.wiley.com/doi/abs/10.1029/JA076i010p02506.

[2] Willis, R., Anderegg, M., Feuerbacher, B., and Fitton, B., "Photoemission and Secondary Electron Emission from Lunar Surface Material," Photon and Particle Interactions with Surfaces in Space, Astrophysics and Space Science Library, Vol. 37, edited by R. Grard, Springer Netherlands, 1973, pp. 389–401. doi:10.1007/978-94-010-2647-5_25, URL http://dx.doi.org/10.1007/978-94-010-2647-5_25.

[3] Zook, H. A., and McCoy, J. E., "Large scale lunar horizon glow and a high altitude lunar dust exosphere," Geophysical Research Letters, Vol. 18, No. 11, 1991, pp. 2117–2120. doi:10.1029/91GL02235, URL http://dx.doi.org/10.1029/91GL02235.

[4] Nitter, T., Havnes, O., and Melandsø, F., "Levitation and dynamics of charged dust in the photoelectron sheath above surfaces in space," Journal of Geophysical Research: Space Physics, Vol. 103, No. A4, 1998, pp. 6605–6620. doi:10.1029/97JA03523, URL http://onlinelibrary.wiley.com/doi/10.1029/97JA03523/abstract.

[5] Abbas, M., Tankosic, D., Craven, P., Spann, J., LeClair, A., and West, E., "Lunar dust charging by photoelectric emissions," Planetary and Space Science, Vol. 55, No. 7-8, 2007, pp. 953–965. doi:10.1016/j.pss.2006.12.007, URL http://www.sciencedirect.com/science/article/pii/S003206330600359X.

[6] Halekas, J. S., Delory, G. T., Brain, D. A., Lin, R. P., Fillingim, M. O., Lee, C. O., Mewaldt, R. A., Stubbs, T. J., Farrell, W. M., and Hudson, M. K., "Extreme lunar surface charging during solar energetic particle events," Geophysical Research Letters, Vol. 34, No. 2, 2007, p. L02111. doi:10.1029/2006GL028517, URL http://onlinelibrary.wiley.com/doi/10.1029/2006GL028517/full.

[7] Wang, J., He, X., and Cao, Y., "Modeling Electrostatic Levitation of Dust Particles on Lunar Surface," IEEE Transactions on Plasma Science, Vol. 36, No. 5, 2008, pp. 2459–2466. doi:10.1109/TPS.2008.2003016.

[8] Poppe, A., and Horányi, M., "Simulations of the photoelectron sheath and dust levitation on the lunar surface," Journal of Geophysical Research, Vol. 115, No. A8, 2010, p. A08106. doi:10.1029/2010JA015286.

[9] Poppe, A., Halekas, J. S., and Horányi, M., "Negative potentials above the day-side lunar surface in the terrestrial plasma sheet: Evidence of non-monotonic potentials," Geophysical Research Letters, Vol. 38, No. 2, 2011, p. L02103. doi:10.1029/2010GL046119, URL http://onlinelibrary.wiley.com/doi/10.1029/2010GL046119/abstract, space Sciences.

[10] Poppe, A. R., "Modeling, Theoretical and Observational Studies of the Lunar Photoelectron Sheath," Ph.D. thesis, University of Colorado, Boulder, 2011.

[11] Halekas, J. S., Delory, G. T., Farrell, W. M. ., Angelopoulos, V., McFadden, J. P., Bonnell, J. W., Fillingim, M. O., and Plaschke, F., "First remote measurements of lunar surface charging from ARTEMIS: Evidence for nonmonotonic sheath potentials above the dayside surface," Journal of Geophysical Research, Vol. 116, No. A7, 2011, p. A07103. doi:10.1029/2011JA016542, URL http://onlinelibrary.wiley.com/doi/10.1029/2011JA016542/abstract, solar and Heliospheric Physics.

[12] Poppe, A. R., Piquette, M., Likhanskii, A., and Horányi, M., "The effect of surface topography on the lunar photoelectron sheath and electrostatic dust transport," Icarus, Vol. 221, 2012, pp. 135–146.

[13] Stubbs, T., Farrell, W., Halekas, J., Burchill, J., Collier, M., Zimmerman, M., Vondrak, R., Delory, G., and Pfaff, R., "Dependence of lunar surface charging on solar wind plasma conditions and solar irradiation," Planetary and Space Science, Vol. 90, 2014, pp. 10–27. doi:10.1016/j.pss.2013.07.008, URL https://www.sciencedirect.com/science/article/pii/S0032063313001876.

[14] Wang, X., Schwan, J., Hsu, H.-W., Grün, E., and Horányi, M., "Dust charging and transport on airless planetary bodies," Geophysical Research Letters, Vol. 43, No. 12, 2016, pp. 6103–6110. doi:10.1002/2016GL069491, URL http://onlinelibrary.wiley.com/doi/10.1002/2016GL069491/full.

[15] Zimmerman, M. I., Farrell, W. M., Hartzell, C. M., Wang, X., Horanyi, M., Hurley, D. M., and Hibbitts, K., "Grain-scale supercharging and breakdown on airless regoliths," Journal of Geophysical Research: Planets, Vol. 121, No. 10, 2016, pp. 2150–2165. doi:10.1002/2016JE005049, URL http://onlinelibrary.wiley.com/doi/10.1002/2016JE005049/abstract.

[16] Zhao, J., Wei, X., Hu, Z., He, X., Han, D., Hu, Z., and Du, X., Photoelectron Sheath near the Lunar Surface: Fully Kinetic Modeling and Uncertainty Quantification Analysis, 2020. doi:10.2514/6.2020-1548, URL https://arc.aiaa.org/doi/abs/10.2514/6.2020-1548.

[17] Han, D., Wang, J., and He, X., "A Nonhomogeneous Immersed-Finite-Element Particle-in-Cell Method for Modeling Dielectric Surface Charging in Plasmas," IEEE Transactions on Plasma Science, Vol. 44, No. 8, 2016, pp. 1326–1332. doi:10.1109/TPS.2016.2580698, URL http://ieeexplore.ieee.org/xpls/abs_all.jsp?arnumber=7506060.

[18] Han, D., "Particle-in-Cell Simulations of Plasma Interactions with Asteroidal and Lunar Surfaces," Ph.D. thesis, University of Southern California, 2015.

[19] Lund, D., Zhao, J., Lamb, A., and Han, D., Fully Kinetic PIFE-PIC Simulations of Plasma Charging at Lunar Craters, 2020. doi:10.2514/6.2020-1549, URL https://arc.aiaa.org/doi/abs/10.2514/6.2020-1549.